Measurement and prediction of machining induced redistribution of residual stress in the aluminium alloy 7449

J.S. Robinson[1], D.A. Tanner[1], C.E. Truman[2], R.C. Wimpory [3]

[1] Materials Surface Science Institute, University of Limerick, Ireland.

[2] Department of Mechanical Engineering, University of Bristol, UK.

[3] Helmholtz Centre Berlin for Materials and Energy, Hahn Meitner Platz 1, Berlin, Germany

Corresponding author

J.S. Robinson

Materials Surface Science Institute,

University of Limerick,

Ireland.

Email; jeremy.robinson@ul.ie

Telephone; +353 61 202240

Fax; +353 61 338172

Abstract

The residual stress distributions in two 7449 aluminium alloy rectilinear blocks have been determined using neutron diffraction. Heat treatment included cold water immersion quenching and a period of precipitation hardening. Quenching induced very high magnitude residual stresses into the two blocks. One block was measured in this condition while the other was incrementally machined by milling to half thickness. Neutron diffraction measurements were made on the milled half thickness block at equivalent locations to the unmachined block. This permitted through thickness measurements from both blocks to be compared, revealing the redistribution of residual stresses induced by machining. A square cross section post in the centre of the machined face was left to act as a stress free reference sample. The distortions arising on the face opposite to that being milled were measured using a co-ordinate measuring machine. The residual stresses and distortion arising in the blocks have been compared to finite element analysis prediction and found to generally agree. Material removal only caused distortion and the residual stresses to redistribute; there was no stress relaxation evident.

Introduction

Polymer composite materials would appear to be replacing aluminium alloys as the major structural material for the latest generation of wide bodied civil passenger aircraft. However, the success of the Airbus A380 which is manufactured mainly with aluminium alloys, confirms that this material remains competitive. Many structural components of the latest aircraft are also fabricated out of heat treatable aluminium alloys as this material continues to offer numerous advantages over fibre reinforced composites. The European collaborative project known as COMPACT (A COncurrent approach to Manufacturing induced Part distortion in Aerospace ComponenTs) was initiated in October 2005. COMPACT has examined manufacturing induced part distortion in aerospace aluminium alloy components. It is estimated that tens of millions of Euro are spent every year in an attempt to either avoid or remedy distortion in components.[1] Part distortion is influenced by residual stress and is caused by the complex relationships between material processing, component design and manufacture.[2] The objective of the COMPACT project was to better understand the multi-functional issues driving part distortion. This paper considers the materials processing aspects of residual stress and their redistribution with machining.

A complex three dimensional residual stress state is introduced into heat treated aluminium product such as plate and forgings by the process of rapid quenching after solution treatment. Thermal gradients act as the driving force for inhomogeneous plastic deformation and it is this that creates the residual stresses upon completion of cooling. For the simple rectilinear shape investigated here, the sequence of residual stress introduction during quenching can be summarised as follows. Immediately upon immersion in the quench media, tensile plastic strains occur initially at the rapidly cooling edges of the block. The plastic zone then expands to cover all the rapidly cooling surfaces. The block at this point consists of a compressed hot and soft interior surrounded by a stretched harder and cooler exterior shell. As the central region starts to cool, it tries to contract but is constrained by the hard outer shell and undergoes tensile plastic deformation. As the block cools further, the magnitude of surface plastic strains diminish as a compressive stress is developed, finally resulting in a surface stressed into compression and a centre into tension.[3] The final stress pattern is a reflection of the geometry of the component and of the temperature gradients generated throughout during the quench. In certain circumstances a different pattern of residual stress can be induced with tensile stresses present at some surfaces. This can occur in components with hollow bores when the internal bore walls are permitted to cool more slowly than the outer surfaces.[4]

In thick aerospace components (t > 75 mm), several researchers have indicated that surface compressive stresses in cold water quenched 7000 series plate and forging alloys can have magnitudes >200MPa using

the mechanical dissection layer removal technique. [5-8] Other investigations using the compliance technique indicates subsurface stress magnitudes >200MPa while surface stresses were approximately 160MPa.[9] The magnitudes of these as quenched residual stresses are such that critical aerospace parts are stress relieved where possible. For simple parts this can be done by applying plastic deformation using stretching or cold compression.[10-13] However for complex shapes, without a constant cross sectional area, this is much more challenging. Distortion[14] can arise after quenching where it can sometimes be corrected by application of small scale local plastic deformation processes known as setting or coining. Part distortion and dimensional instability can also occur during subsequent machining as the component self equilibrates to compensate for the unbalancing of forces and moments as material is removed.[15] How residual stresses actually redistribute during machining has received only little scientific attention. The aim of this investigation was to characterise the redistribution for a simple rectilinear shape, and determine how this redistribution influences distortion. The residual stresses remaining in a rectilinear aluminium block after the sequential removal of 50% of the original thickness of the block have been determined by neutron diffraction. The procedure followed was not unlike that undertaken in a layer removal experiment first described by Treuting and Read.[16] The redistributed residual stresses are compared to predictions using finite element methods.

Experimental

Material details

The two blocks used in this experiment were both extracted from a large (830 kg), approximately rectilinear forging manufactured by Mettis Aerospace Ltd, UK. The two blocks were initially contiguous within the forging. The composition of the 7449 alloy is given in Table 1. The individual block dimensions prior to heat treatment were 136 mm (L-longitudinal) x 160 mm (LT-long transverse) x 120 mm (ST-short transverse) where the orientations refer to those of the original primary working direction of the forging, as shown in Figure 1. The long transverse direction has been arbitrarily designated *x*, the longitudinal *y* and the short transverse *z*. The blocks were solution heat treated at 470±5°C for 4 hours and then rapidly quenched by immersing in cold water with accompanied vigorous agitation (water temperature < 20°C). The blocks were heat treated sequentially. Each block had a mass of approximately 7 kg with a surface area of 0.11m^2. The Biot number estimated for the cold water quench was approximately 1.5 which is indicative of significant thermal gradients during cooling. This number was calculated using a characteristic linear dimension for the forgings of 23 mm, an average thermal conductivity of 180 $Wm^{-1}K^{-1}$ and an average heat transfer coefficient of 12,000 $Wm^{-2}K^{-1}$ calculated from quenching experiments. As natural aging would lead to a time dependent change in the lattice parameter, the alloy was stabilised microstructurally by artificially aging for 24 hours at 120°C. This would be expected to induce a small (<20%) reduction in the residual stress compared to the as quenched condition. The microstructure of the block consisted of approximately rod shaped grains elongated into the longitudinal direction with a typical grain length being <1000 μm. In the transverse directions as shown in Figure 2, the grain characteristic dimension was <200 μm. Within these grains a substructure was observed consisting of well defined polygonised equiaxed subgrains. The diameter of the subgrains was <20 μm. Other coarse phases noted were fragmented Al-Cu-Fe constituent particles and a very small volume fraction of undissolved $MgZn_2$.

Machining procedure and measurement of distortion

One of the blocks (labelled Z2RA) was left in the heat treated condition while block Z2RB was subject to dimensional measurement and machining by vertical milling. A Brown and Sharpe MVAL PFX 4-5-4 coordinate measurement machine (CMM, accurate to ± 1 μm) was used prior to milling to measure the flatness of one face of Z2RB bounded by the *x* and *y* directions. 25 measurements were made, encompassing the majority of the surface area of the face. The block was then clamped around the

measured face and placed into a 3 axis Hurco Ultimax CNC machining centre. Material was removed in 10mm increments where the thickness was the z direction of the block. This was carried out in two passes of the milling cutter (axial depth of cut of 5 mm). The spindle speed was 8600 rpm, with a surface speed of 3600 mm/min. The high speed machining cutter had 3 flutes, a diameter of 25 mm and an end radius of 5 mm. The step over during machining was 20 % of the diameter of the cutter (5 mm). The machining procedure and cutter end radius were chosen to minimise the introduction of residual stresses by the milling process itself as described by Denkena and de León.[17]

The cutter path followed permitted the retention of a square cross section post of side 10 mm in the centre of the face, as shown in Figure 1. This was subsequently used as a strain free reference sample during the neutron diffraction measurements. After removal of each 10 mm increment of material, the opposite, parallel, unmachined face of the block was re-measured on the CMM to determine the displacement of the plane in the surface bounded by the *x* and *y* directions of the block.

Residual stress and distortion prediction using FEA

ABAQUS[18] finite element code was used to predict the residual stress distribution after cold water quenching. The rectilinear block was considered to be isotropic with dimensions of 120(*z*, ST)*160(*x*, LT)*136(*y*, L) mm with one-quarter of the block modelled to take advantage of symmetry conditions. The initial geometry of the one-quarter model was 120(*z*, ST)*80(*x*, LT)*68(*y*, L) at 470°C. For the model, 5760 eight-noded quadratic brick elements were used as determined through mesh density experiments (heat transfer – type DC3D8; stress displacement – type C3D8).

The analysis method employed by ABAQUS to predict residual stress distributions from quenching is uncoupled in that the temperature and displacement problems are solved consecutively. Results from the thermal analysis are read at the beginning of the stress/displacement analysis and provide the displacement loading through thermal contraction. This thermal contraction results in the development of elastic and plastic strains from which residual stresses can be calculated.

Heat transfer analysis

Temperature dependent properties for specific heat capacity (C_p)[19], thermal conductivity (k)[20] and density (ρ)[5] are all readily available in literature for aluminium alloys. The heat transfer coefficient (h) acts as the main boundary condition on the finite element model as it determines the rate at which heat leaves the block surface. As this parameter varies for different quenchant temperatures and conditions, it was calculated using an inverse technique with both INTEMP[21] and ABAQUS software, resulting in the same curve in both cases.. Comparison of experimental and predicted cooling curves for different rectilinear blocks of aluminium alloys has indicated that the heat transfer model accurately predicts cooling during the quench.

Stress-displacement analysis

Values for the thermal expansion coefficient (α_{th})[22], elastic modulus (E)[23] and Poisson's ratio (v)[23] of alloys similar to 7449 were taken from literature. The elastic modulus and the thermal expansion coefficient were input as a function of temperature while Poisson's ratio was assumed to remain constant. During the quenching of aluminium alloys, the material is plastically deformed at low strain rates, the degree of which determines the final magnitude of residual stress. Unlike the elastic behaviour, the flow stress of 7449 is strain rate dependent. Knowledge of the deformation behaviour of 7449 at varying strain rates and temperatures up to 470°C is not widespread, and thus a compromise was reached in this model by using flow stress values obtained from torsion tests on 7150.[24]

At high temperatures, the material can be assumed to be strain rate dependent and follow a perfectly plastic stress–strain curve. As temperatures approach room temperature strain rate dependency begins to become negligible and work hardening begins to influence the stress-strain response of the material. Therefore, the input data was modified to incorporate work hardening and is assumed to be strain rate independent at room temperature. This is achieved through use of tensile test data measured for 7010 directly after quenching.

Layer removal analysis

After predicting the stress distribution after quenching, layers of elements (thickness 5 mm) were removed successively from one surface as described for the experimental case, and the resultant distortion in the z direction was predicted on the opposing surface. Positive deflection was defined as deflection away from the centre of curvature. The finite element model did not account for any machining induced stresses caused by material removal.

Residual stress measurements

Residual stresses were determined using the strain scanner instrument known as STRESS SPEC located at the FRM II at the TUM in Munich, Germany. [25, 26] Measurements were made following the guidelines present in [27, 28]. The wavelength of the monochromatic radiation was 1.74Å and the nominal sampling gauge volume was set at 3x3x3 mm^3 as defined by the incident and diffracted slit widths. The position of the aluminium {311} peak was measured by the diffractometer. The incident and diffracted slits were positioned as close to the gauge volume as possible to minimise optical aberrations such as peak clipping [29]

Positions within a quarter of the volume of Z2RA were sampled and the same measurement locations were used for Z2RB so that the measurements could be directly compared. This meant that half of the volume of Z2RB was sampled. Measurement locations are shown in Figure 1. The volume sampled was split into six *y*-*z* planes and twenty five measurement locations were located on each plane making for a total of one hundred and fifty measurements per block. The strain at each location was measured in three orthogonal directions corresponding to the primary working directions of the forging. These directions were assumed to be the principal stress directions due to them being parallel to the directions of maximum heat flow during quenching. Lattice spacings were converted to residual strains and stresses using the standard three dimensional Hooke's law as shown in the equations below.[30] A Young's modulus of 70 GPa and a Poisson's ratio of 0.3 was used in all the calculations.

$$\sigma_{xx} = \frac{E}{1+\nu}\varepsilon_{xx} + \frac{E\nu}{(1+\nu)(1-2\nu)}\left(\varepsilon_{xx} + \varepsilon_{yy} + \varepsilon_{zz}\right) \quad (1)$$

$$\sigma_{yy} = \frac{E}{1+\nu}\varepsilon_{yy} + \frac{E\nu}{(1+\nu)(1-2\nu)}\left(\varepsilon_{xx} + \varepsilon_{yy} + \varepsilon_{zz}\right) \quad (2)$$

$$\sigma_{zz} = \frac{E}{1+\nu}\varepsilon_{zz} + \frac{E\nu}{(1+\nu)(1-2\nu)}\left(\varepsilon_{xx} + \varepsilon_{yy} + \varepsilon_{zz}\right) \quad (3)$$

The strain free reference sample (for measuring d_{311}^{0}) consisted of the square section post left in the centre of the milled face of Z2RB. The post was separated from the block prior to any neutron diffraction measurements to form a right square prism of material. Multiple measurements of the {311} interplanar spacing in three orthogonal directions were made along the centreline of the prism in its long axis; *z*

direction. A minor microstructural change was expected to occur in the strain free sample as the cooling rate during quenching varied from one end of the post to the other.[31]

Results

Distortion caused by material removal, Measurement and prediction.

Measurement of the position of points on the surface of Z2RB bounded by the *x* and *y* directions after heat treatment confirmed that the face was flat to within 0.8 mm. This was an as forged surface and as plastic flow occurs during quenching, this had caused slight bulging out at the centre of the exterior faces.

As material was incrementally removed from one side of Z2RB, the maintenance of equilibrium resulted in a bending moment that distorted the block. This resulted in the surface being measured becoming convex. Figure 3 indicates how a corner and centre location were displaced as material was removed from the opposite face. The displacement was relatively symmetrical with all four corners of the block being displaced down as the block centre was raised up to form the convex surface. The corner displacements in Figure 3 are displayed as the mean the displacements of all four corner of the block. The error bars correspond to ± 1 standard deviations of the mean of the four corner displacements. The displacement prediction by the finite element model for these two locations is also shown in Figure 3. The distortion of the measured surface of Z2RB compared with the finite element prediction is shown in Figure 4. This figure illustrates the final surface after removal of a thickness of 60 mm. The actual block was measured to within 10 mm of the edges.

Strain free reference sample

With a Biot number of 1.5, the quench resulted in significant thermal gradients within the blocks. The strain free reference sample was an integral part of Z2RB during quenching and was separated from the block only after completion of machining. As such it was expected to be microstructurally representative of both Z2RA and B. It was also assumed it would be approximately strain free due to the complete removal of the surrounding constraining material. The difference in the FEA predicted cooling rates of the surface compared to the core for locations in the block corresponding to both ends of the strain free sample are shown in Figure 5. The difference in cooling rate is relatively small as illustrated by Figure 6. This figure superimposes the predicted cooling curves on the time temperature iso-hardness curves (C curves) for over aged 7449. The time temperature property curves were developed following the procedure in [32]. It can be seen that there is only a small reduction in the hardening (precipitation) potential of material located at the core compared to the surface.

The neutron diffraction peak position (2θ) as a function of location along the strain free reference sample (measuring d_{311}^{0}) is shown in Figure 7 with peak position converted to microstrain (ε x 10^{-6}) by assuming a single average d_{311}^{0}. (The surface exposed to the quench water corresponds to the 0 mm position in the figure). If significant microstructural variation existed along the post due to the different cooling, (causing different degrees of solute supersaturation), this would be reflected in a shift in the peak position, but apart from the shift when the gauge volume enters and exits the sample, the lattice parameter did not vary significantly either with position or orientation of measurement. This permitted the use of a single average d_{311}^{0} which was used to calculate ε_{xx}, ε_{yy} and ε_{zz} . The cause of the peak shift when the gauge volume is partly outside the sample is well documented. [33]

Residual stress measurement in Z2RA

The residual stress distribution in the unmachined Z2RA block varied from highly biaxial compression in the surface to triaxial tensile in the centre of the block. The maximum compressive stress determined by neutron diffraction was -184 MPa while the maximum tensile stress was 213 MPa. The average error in the residual stresses arising from the {311} diffraction peak fitting was ±10 MPa.

Figure 8 displays the σ_{XX} residual stresses in blocks Z2RA and Z2RB as six *y-z* contour maps corresponding to the measurement locations shown in Figure 1. The lower six contour maps correspond to the unmachined block, Z2RA while the upper six contour maps correspond to the machined block, Z2RB. The contours maps are depicted as isometric views situated on a rectangular base representing the plan view of the relevant block. The σ_{YY} and σ_{ZZ} residual stresses are shown in Figure 9 and Figure 10 respectively.

For block Z2RA, the σ_{XX} residual stresses on the *y-z* planes where *x* = 5 mm and *x* = 155 mm can be seen to be close to zero. This was the expected result as these planes are close to the free surfaces of the block in the *x* direction. In Figure 9 it is observed that the σ_{YY} residual stresses approach zero toward the free surface in the y direction and the same pattern is repeated in Figure 10 for the σ_{ZZ} residual stresses in the z direction. The external surfaces of the block were all subject to a large biaxial compressive residual stress of magnitude in the range -156 MPa to -184 MPa. These observations are in reasonable agreement with other researchers that have used neutron diffraction [34, 35], the contour method [36], crack compliance [9, 37], layer removal [5, 8] and centre hole drilling [38, 39]. It is clear from these three figures that the expected pattern of residual stress has been confirmed by the neutron diffraction measurements; an exterior stressed in compression balanced by an interior stressed into triaxial tension. The tensile σ_{XX} residual stresses in the centre of the block reached a maximum magnitude of σ_{XX} = 213 MPa. This stress acted in the longest dimension of the quenched block. The maximum magnitudes of the σ_{YY} and σ_{ZZ} residual stresses in the centre of the block were 169 MPa and 92 MPa respectively.

The variation of residual stress through the thickness of Z2RA is illustrated in Figure 11 where ten adjacent (x = 65 and x = 95 mm) measurement locations are chosen for z = 55 mm. The associated σ_{YY} σ_{XX} and σ_{ZZ} residual stresses are plotted as a function of position in the y direction. Figure 11 shows the general trend of changing residual stress with position into block Z2RA (open symbols).

Another observation that can be made which reflects the apparent quality of these observations is the obvious symmetry in the two block eighths measured. Perfect symmetry in the residual stress distribution is unlikely when cold water quenching due to local variations of the heat transfer coefficient caused by surface finish variations and chaotic variations in convection, but it is clear from these data that the determined variation from eighth to eighth is quite small.

As a final check on the quality of the residual stress measurements within Z2RA, a force balance was conducted on selected cross sections where the normal stress on the planes changed from highly compressive to highly tensile. Assumptions involving extrapolation had to be made about the residual stress distribution around the unmeasured periphery of the block and when these were taken into consideration, the distributions determined by neutron diffraction were found to be in equilibrium (typically always within 14% of being balanced).

Residual stress measurements in Z2RB

The residual stresses in Z2RB were determined by neutron diffraction after completion of machining and removal of the strain free reference sample. The measurement locations were equivalent to the same positions as Z2RA as shown in Figure 1.

The residual stress redistribution was complex. The upper six contour maps in Figure 8 depict the σ_{XX} residual stresses in the machined block, Z2RB. The maximum σ_{XX} residual stress was 120 MPa (a decrease of 43% compared to Z2RA) with the minimum being -227 MPa (changed from -184 MPa; an increase in magnitude of 24%). Compared to Z2RA, the locus of the tensile core has moved so that it remains encapsulated within the block. The large magnitude x-y surface σ_{XX} residual stresses present in the unmachined block were also significantly reduced from -138 MPa to close to zero.

In Figure 9 the σ_{YY} residual stresses remaining in Z2RB are shown. Similarly, the locus of the maximum tensile stress has moved with the core of the block. The x-y surface compressive residual stresses have also been reduced by over 100 MPa. The maximum residual stress in the tensile core has reduced from in 169 MPa in Z2RA to 95 MPa in Z2RB, a change of 44%. The compressive stresses close to the y-z exterior surfaces (x = 5 and x = 155 mm) remained relatively unchanged. The greatest change in the compressive residual stresses was from -168 MPa in Z2RA to -215 MPa in Z2RB; a 28% increase in magnitude.

The σ_{ZZ} residual stresses are shown in Figure 10. A large change was observed in these stresses as they were acting in the direction expected to be most affected by the removal of material. The maximum residual stress in the tensile core was reduced from 92 MPa in Z2RA to 54 MPa in Z2RB. The greatest change in the compressive residual stresses was from -183 MPa in Z2RA to -72 MPa in Z2RB; a 60% decrease in magnitude. Residual stresses close to the new machined surface were close to zero. The redistribution of σ_{ZZ} resulted in significant reduction of the size of the stress gradients in this direction with the residual stresses in the majority of locations being close to zero.

FEA prediction of residual stress

The predicted orthogonal quench-induced residual stress distributions present in the unmachined block are shown in the lower contour maps of Figure 12, Figure 13, and Figure 14. These figures can be compared to the lower maps in Figure 8, Figure 9, and Figure 10. The distribution of the residual stresses was in agreement with the neutron diffraction measurements. The magnitudes for specific locations were not the same however, with the FEA predicting a greater range of residual stress, ie compressive stressed regions indicated higher magnitude compressive stresses and tensile regions higher magnitude tensile. For example, the predicted σ_{YY} and σ_{ZZ} components close to the surface where x= 5 mm (and 155 mm) were -199 and -196 MPa respectively. The residual stresses determined in these same locations were σ_{YY} = 167 MPa and σ_{ZZ} = -173. In the tensile core the differences were more apparent with predicted stresses exceeding the determined by approximately 60 MPa for all three orthogonal directions. Comparing all the neutron diffraction residual stresses to the nearest equivalent location for the FEA predictions, the average differences were σ_{XX} = -12 MPa (1 standard deviation = 36 MPa), σ_{YY} = 6 MPa (1 standard deviation = 35 MPa) and σ_{ZZ} = 9 MPa (1 standard deviation = 41 MPa). The relatively large standard deviations reflect the variability of the differences between determined and predicted. For the machined block the FEA again successfully predicted a similar pattern of redistribution to that determined by the neutron diffraction measurements. Predicted residual stresses were again of greater magnitude compared to those determined by neutron diffraction, and by a similar margin to the as quenched block.

Discussion

Characterisation of the residual stresses in the unmachined block Z2RA is consistent with the usually reported pattern of surface compression balanced by subsurface tension. The magnitude and distribution of these residual stresses are in accordance with other investigations. The magnitudes of the maximum and minimum stresses observed are lower than previous investigations conducted on the aluminium alloy 7449 because the blocks differ in size [40], and blocks Z2RA and Z2RB were both aged for 24 hours at 120°C prior to machining (of Z2RB) and the neutron diffraction measurements. Artificial ageing, used to

precipitation harden the alloy, induces a small but significant reduction in residual stress.[41] Machining Z2RB results in redistribution of the residual stresses and distortion of the block. The distortion was monitored using a CMM machine and compared to predictions made using a finite element model. The prediction is in close agreement with the experimental observations. This suggests that the finite element quench modelling and residual stress field prediction are both accurate and that the assumptions made in the finite element model about redistribution of residual stress during material removal are satisfactory. Characterisation of the residual stresses in the machined block was also possible by neutron diffraction. Despite machining into a highly tensile region of Z2RB the tensile stresses were not exposed and always remained subsurface. There is limited evidence that tensile stresses can be exposed[4] but this was not found here for the simple geometry investigated. The FEA predicts the correct pattern of residual stress in the as quenched block but the actual magnitudes are not identical. Reasons for the discrepancy can be attributed to the use of 7150 data for the elevated temperature thermomechanical properties and 7010 data for the room temperature work hardening. These alloys are chemically similar to 7449 in that they are all Al-Zn-Mg-Cu alloys but it is reasonable to expect the plastic flow of 7449 to be somewhat different when quenched. In addition the neutron diffraction measurements were made by sampling a gauge volume in regions where there were significant strain gradients, resulting in an averaging effect of the measured strain.

One question that does arise is the possibility that actual stress relaxation occurs as a consequence of machining and not just residual stress redistribution. This would require additional yielding and subsequent plasticity to take place as a consequence of material removal. This is an unlikely scenario bearing in mind the age hardened condition of the alloy. However, this supposition can be tested by calculating the stored elastic strain energy density of the block prior to machining and after machining. The strain energy density for an elastically deformed isotropic solid obeying Hooke's law is shown in equation (4). The form used to calculate the strain energy from the measured and predicted residual strains which are assumed principal is shown in equation (5).

$$U = \frac{1}{2}\left(\sigma_{xx}\varepsilon_{xx} + \sigma_{yy}\varepsilon_{yy} + \sigma_{zz}\varepsilon_{zz} + \tau_{xy}\gamma_{xy} + \tau_{yz}\gamma_{yz} + \tau_{zx}\gamma_{zx}\right) \quad (4)$$

$$U = \frac{E}{2}\left(\varepsilon_{xx}{}^{2} + \varepsilon_{yy}{}^{2} + \varepsilon_{zz}{}^{2}\right) \quad (5)$$

The total elastic strain energy density *U* calculated from the orthogonal strains measured by neutron diffraction for the as quenched block Z2RA was 134 kJ m^{-3}. For the machined block, Z2RB, *U* was 67 kJ m^{-3}. The elastic strain energy density calculated from the FEA predicted orthogonal strains was 120 kJ m^{-3} for Z2RA and 60 kJ m^{-3} for the machined block Z2RB. Both experimental data and prediction confirm that, in this investigation at least, there is no residual stress relaxation associated with the removal of material, only redistribution. If the principal strains output from the FEA model are used to calculate the strain energy density, a significantly larger value results; 200 kJ m^{-3}. This is a consequence of the FEA model indicating that in fact the orthogonal strains are not always principal and the additional strain energy contribution arises from non zero shear strains. Regions close to edges and corners of the blocks are where the assumption that orthogonal strains are principal breaks down.

One further speculative conjecture emerges from this research. Over recent years there has been widespread discussion whether machining processes may cause part distortion in the absence of a pre-existing residual stress field. The results provided in this paper demonstrate that residual stress redistribution, rather than relaxation, is the driver for part distortion. Recognising that machining operations impart only near-surface residual stress distributions in components (typically up to a maximum depth of around 2mm). This would suggest machining may cause part distortion (in the absence of a pre-

existing residual stress field) only if the machined part is thin in relation to the maximum depth of the residual stress field it induces. In other words, we postulate that common machining processes may distort work pieces that are up to several millimetres thick, but cause no distortion for thicker specimens.

Conclusions

Predicting an accurate residual stress distribution within 7449 blocks caused by cold water quenching has been demonstrated using finite element analysis. In this investigation, the FEA tends to exaggerate the magnitude of the residual stresses compared to the neutron diffraction measurements, but this can be attributed in part to the use of non optimised material properties and the fact the actual blocks were artificially aged which would have caused some stress relaxation.

The residual stress distribution in cold water blocks is confirmed as being highly compressive in the surface balanced by subsurface tension.

Machining away half of one cold water quenched blocks resulted in distortion in conjunction with redistribution of the residual stress. Tensile stresses were not exposed in the machined block with the locus of the tensile core moving to remain encapsulated within the machined block.

FEA has also shown to be able to predict the distortion and redistribution of residual stress when material is removed in layers from a cold water quenched block.

For the size of block used here, the use of a single strain free reference value was feasible for the neutron diffraction measurements as the 7449 alloy was not quench sensitive enough to give rise to significant microstructural gradients through the thickness of the block.

Machining the block only caused the redistribution of residual stresses. No stress relaxation was encountered as demonstrated by strain energy density calculations for the machined and unmachined blocks.

Acknowledgements

This investigation has been supported by the European Commission under the 6th Framework Programme project known as COMPACT (AST4-CT-2005-516078), which contributes to the thematic priority “Strengthening Competitiveness” of the European aircraft industry. The residual stress measurements conducted on the STRESS-SPEC instrument at FRM II have also been supported by the European Commission under the 6th Framework Programme through the Key Actions: Strengthening the European Research Area, Research Infrastructures. Contract n°: RII3-CT-2003-505925.

References

1. Sim, W.M., *Challenges of residual stress and part distortion in the civil airframe industry*, in *2nd International Conference on Distortion Engineering*. 2008: Bremen, Germany.

2. Brinksmeier, E., J. Solter, and C. Grote, *Distortion engineering - Identification of causes for dimensional and form deviations of bearing rings.* Cirp Annals-Manufacturing Technology, 2007. **56**(1): p. 109-112.

3. Tanner, D.A., J.S. Robinson, and R.L. Cudd, *Relief of residual stresses in aluminium alloy 7010*, in *Proceedings of the The Sixth International Conference on Residual Stresses ICRS-6, 10-12 July 2000*. 2000, Institute of Materials: Oxford, UK. p. 1299-1306.

4. Barker, R.S. and G.K. Turnbull, *Control of residual stresses in hollow aluminium forgings.* Metal Progress, 1966. **Nov.**: p. 60-65.

5. Jeanmart, P. and J. Bouvaist, *Finite element calculation and measurement of thermal stresses in quenched plates of high-strength 7075 aluminium alloy.* Materials Science and Technology, 1985. **1**: p. 765-769.

6. Yazdi, S.R., D. Retraint, and J. Lu, *Study of through-thickness residual stress by numerical and experimental techniques.* Journal of Strain Analysis for Engineering Design, 1998. **33**(6): p. 449-458.

7. Yoshihara, N., et al., *Development of large high strength aluminium alloy component for spacecraft.* NKK Technical Review, 1992. **64**: p. 21-27.

8. Boyer, J.C. and M. Boivin, *Numerical calculations of residual stress relaxation in quenched plates.* Materials Science and Technology, 1985. **1**: p. 786-792.

9. Prime, M.B. and M.R. Hill, *Residual stress, stress relief, and inhomogeneity in aluminum plate.* Scripta Materialia, 2002. **46**(1): p. 77-82.

10. Altschuler, Y., T. Kaatz, and B. Cina, *Mechanical Relaxation of Residual Stresses*, in *ASTM STP 993*. 1988. p. 19-29.

11. Bains, T. *Residual stress reduction in aluminum die forgings*. in *1st International Non-Ferrous Processing and Technology Conference*. 1997. St. Louis, Missouri, USA: ASM International.

12. Nickola, W.E., *Residual Stress Alterations via Cold Rolling and Stretching of an Aluminum Alloy*, in *ASTM STP 993*. 1988. p. 7-18.

13. Vohringer, O., *Relaxation of residual stresses by annealing or mechanical treatment*, in *Advances in Surface Treatments Technology-Applications-Effects*, A. Niku-Lari, Editor. 1987, Pergamon Press. p. 367-396.

14. Becker, R., et al., *Distortion and residual stress in quenched aluminum bars.* Journal of Applied Mechanics-Transactions of the Asme, 1996. **63**(3): p. 699-705.

15. Lynch, J.J. *The measurement of residual stresses*. in *Thirty-third National Metal Congress and Exposition*. 1951. Detroit: American Society of Metals.

16. Treuting, R.G. and W.T. Read, *A Mechanical Determination of Biaxial Residual Stress in Sheet Materials.* Journal of Applied Physics, 1951. **22**(2): p. 130-134.

17. Denkena, B. and L. de León, *Machining induced residual stress and distortion in forged aluminium parts*, in *8th International Conference on Advanced Manufacturing Systems and Technology (AMST'08)*. 2008: Udine, Italy.

18. Hibbitt, Karlsson, and Sorensen, *ABAQUS Users Manual*. 2009: Providence, RI.

19. Touloukian, Y.S. and H. Buyco, *Specific heat: Metallic elements and alloys*, in *Thermophysical properties of matter*. 1970, IFI/Plenum Press: New York.

20. Touloukian, Y.S., et al., *Thermal Conductivity: Metallic elements and alloys*, in *Thermophysical properties of matter*. 1970, IFI/Plenum Press: New York.

21. Trujillo, D.M., *INTEMP*. 2003, TRUCOMP: FOUNTAIN VALLEY, CA., 92708, USA. p. Inverse Heat Transfer Analysis.

22. Touloukian, Y.S., et al., *Thermal expansion: Metallic elements and alloys*, in *Thermophysical properties of matter*. 1970, IFI/Plenum Press: New York.

23. Handbook, M., *Heat Treating*, in *Metals Handbook*. 1981, ASM International. p. 696-697.

24. Jackson, A., *Homogenisation effects on the hot working of Al-Zn-Mg-Cu alloys*. 1992, University of London: London.

25. Hofmann, M., et al., *The new materials science diffractometer STRESS-SPEC at FRM-II.* Physica B-Condensed Matter, 2006. **385-86**: p. 1035-1037.

26. Hofmann, M., et al., *Scientific Review: Stress Spec: Advanced Materials Science at the FRM II.* Neutron News, 2007. **18**(4): p. 27 - 30.

27. IS0/TTA3, *Polycrystalline materials – Determination of residual stresses by neutron diffraction*, in *Technology trends assessment*. 2001, International standardisation organisation.

28. 21432, D.C.I.T., *Non-destructive testing. Standard test method for determining of residual stresses by neutron diffraction*. 2005, British Standards Institute.

29. Pirling, T., D.J. Hughes, and J.S. Robinson, *Precise Determination Of Residual Stresses In Large Specimens*, in *5th International Conference on Mechanical Stress Evaluation by Neutrons and Synchrotron Radiation (MECA SENS V)*. 2009: Mito, Japan.

30. Hutchings, M.T., et al., *Introduction to the characterisation of residual stress by neutron diffraction*. 2005, Boca Raton, FL, USA: CRC Press. 424.

31. Steuwer, A., et al., *The variation of the unstrained lattice parameter in an AA7010 friction stir weld.* Acta Materialia, 2007. **55**(12): p. 4111-4120.

32. Flynn, R.J. and J.S. Robinson. *The application of advances in quench factor analysis property prediction to the heat treatment of 7010 aluminium alloy*. in *Proceedings of the International Conference on Advances in Materials and Processing Technologies, AMPT2003*. 2003. Dublin City University, Dublin, Ireland.

33. Webster, P.J., et al., *Impediments to efficient through-surface strain scanning.* Journal of Neutron Research, 1996. **3**(4): p. 223 - 240.

34. Walker, D.M. and R.Y. Hom, *Residual stress analysis of aircraft aluminum forgings.* Advanced Materials & Processes, 2002. **160**(6): p. 57-60.

35. Koc, M., J. Culp, and T. Altan, *Prediction of residual stresses in quenched aluminum blocks and their reduction through cold working processes.* Journal of Materials Processing Technology, 2006. **174**(1-3): p. 342-354.

36. Prime, M.B., M.A. Newborn, and J.A. Balog. *Quenching and cold-work residual stresses in aluminium hand forgings: contour method measurement and FEM prediction*. in *THERMEC'2003: Processing & Manufacturing of Advanced Materials*. 2003. Madrid, Spain.

37. Wang, Q.C., et al., *Evaluation of residual stress relief of aluminum alloy 7050 by using crack compliance method.* Transactions of Nonferrous Metals Society of China, 2003. **13**(5): p. 1190-1193.

38. Lin, G.Y., et al., *Residual stress in quenched 7075 aluminum alloy thick plates.* Transactions of Nonferrous Metals Society of China, 2003. **13**(3): p. 641-644.

39. Zhang, H., et al., *Influence of quenchant factors on residual stresses in quenched 7075 aluminium-alloy thick plate.* Heat Treatment of Metals, 2003. **30**(3): p. 61-64.

40. Robinson, J.S., et al., *Influence of cold compression on the residual stresses in 7449 forgings.* Advances in X-ray Analysis, 2009. **52**: p. 667-674.

41. Davis, J.R., G.M. Davidson, and S.R. Lampman, *Heat treating of aluminum*. Vol. 4. 1995: ASM International. 841-879.

List of Table Captions

Table 1 Specification alloy chemistry and chemical analysis results, wt%

List of Figures Captions

Figure 1 Neutron diffraction measurement locations for the unmachined and machined blocks. Machined block indicates the location of the strain free post of material.

Figure 2 Microstructure of the 7449 alloy. The horizontal corresponds to the y (LT) direction and the vertical the z (ST) direction.

Figure 3 Cumulative displacement of two locations on the unmachined face of Block Z2RB as material is removed from the opposite face. CMM measurements compared to finite element prediction. Error bars for the CMM corner curve correspond to ±1 standard deviations for the mean of all four corner displacements.

Figure 4 Distortion caused by removal of material to a depth of 60 mm (a) and corresponding FEA prediction (b)

Figure 5 Predicted cooling curves and cooling rates during cold water quenching of one end of the strain free reference sample (surface) compared to the other (core).

Figure 6 Time temperature transformation curves for the 7449 alloy. Each curve represents an iso-hardness curve for an over aged condition. Superimposed are the predicted cooling curves for the surface and core of the block during cold water quenching

Figure 7 Strain free reference sample peak position displayed as variation of microstrain for the three orthogonal orientations

Figure 8 The σ_{XX} residual stresses in the unmachined block Z2RA (lower contour maps), and Z2RB (upper contour maps).

Figure 9 The σ_{YY} residual stresses in unmachined Z2RA (lower contour maps), and Z2RB (upper contour maps).

Figure 10 The σ_{ZZ} residual stresses in unmachined Z2RA (lower contour maps), and Z2RB (upper contour maps).

Figure 11 Variation of residual stress with position in the y (L) direction of block Z2RA and block Z2RB

Figure 12 The FEA predicted σ_{XX} residual stresses in the unmachined block Z2RA (lower contour maps), and Z2RB (upper contour maps).

Figure 13 The FEA predicted σ_{YY} residual stresses in the unmachined block Z2RA (lower contour maps), and Z2RB (upper contour maps).

Figure 14 The FEA predicted σ_{ZZ} residual stresses in the unmachined block Z2RA (lower contour maps), and Z2RB (upper contour maps).

List of Tables

Table 1 Specification alloy chemistry and chemical analysis results, wt%

Alloy	Si	Fe	Cu	Mn	Mg	Zn	Ti+Zr	Al
7449	0.12 max	0.15 max	1.4-2.1	0.20 max	1.8-2.7	7.5-8.7	0.25 max	Bal.
7449 (ca)	0.06	0.08	2.02	0.01	1.92	8.39	0.138	Bal.

List of Figures

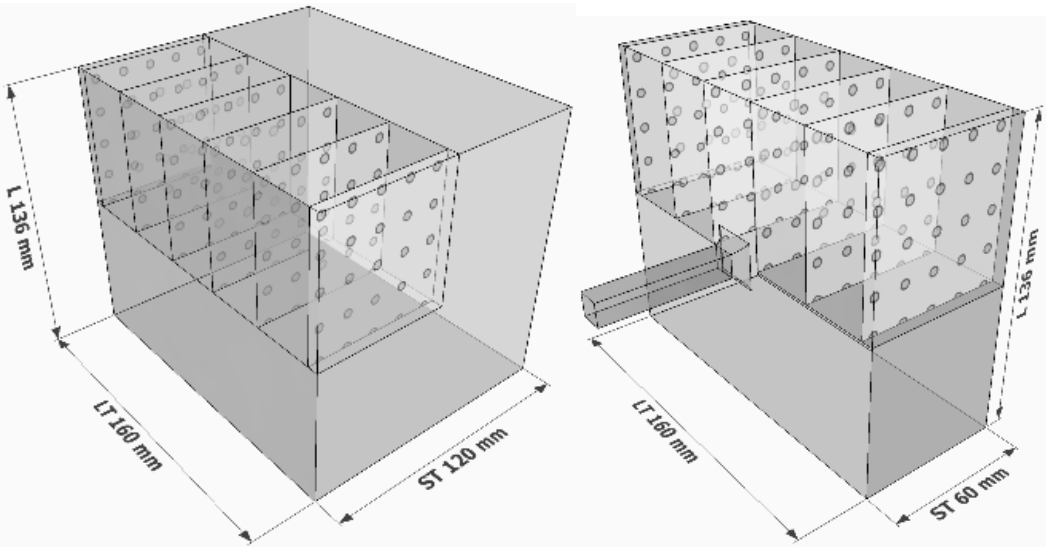

Figure 1 Neutron diffraction measurement locations for the unmachined and machined blocks. Machined block indicates the location of the strain free post of material.

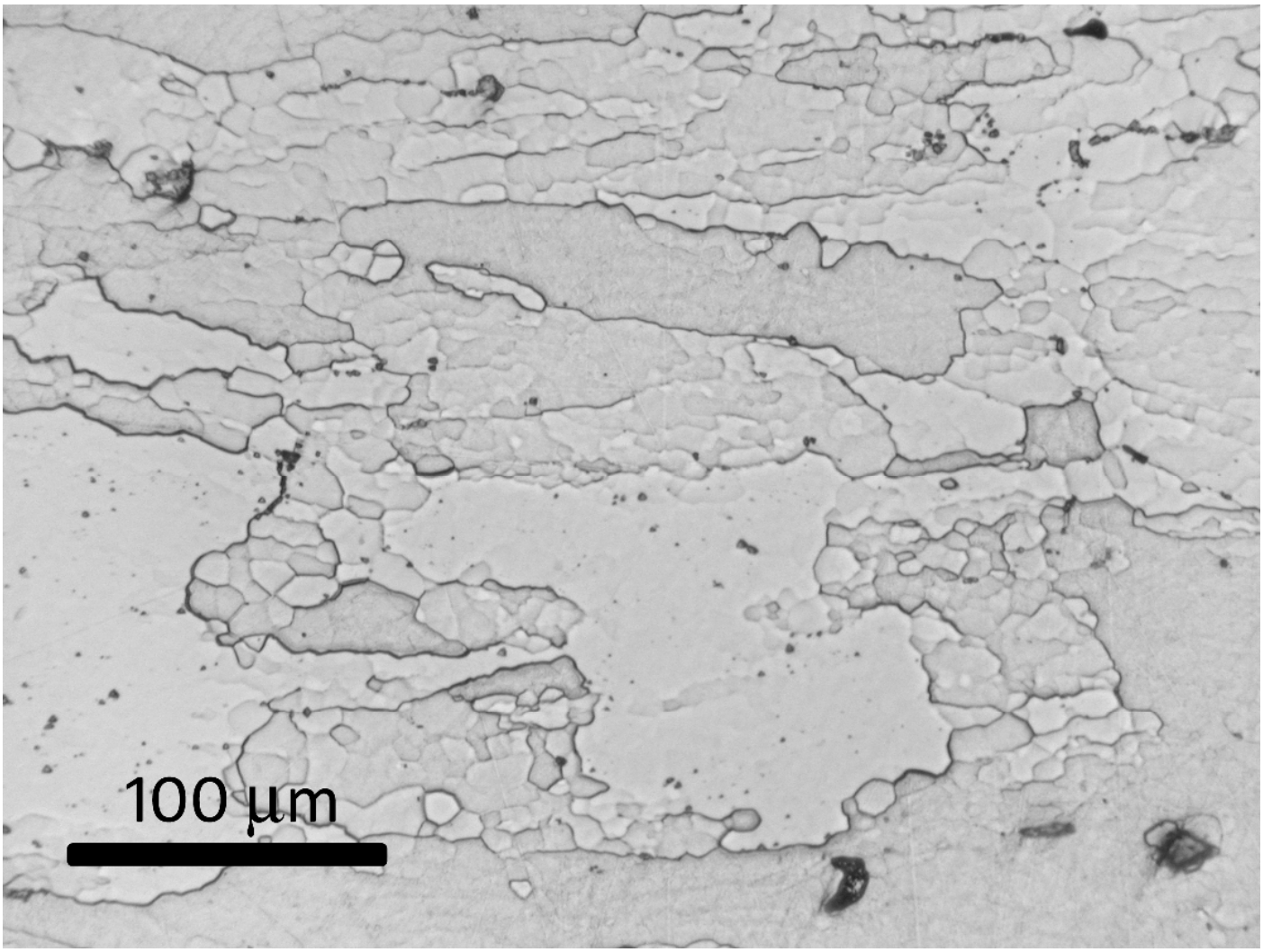

Figure 2 Microstructure of the 7449 alloy. The horizontal corresponds to the y (LT) direction and the vertical the z (ST) direction.

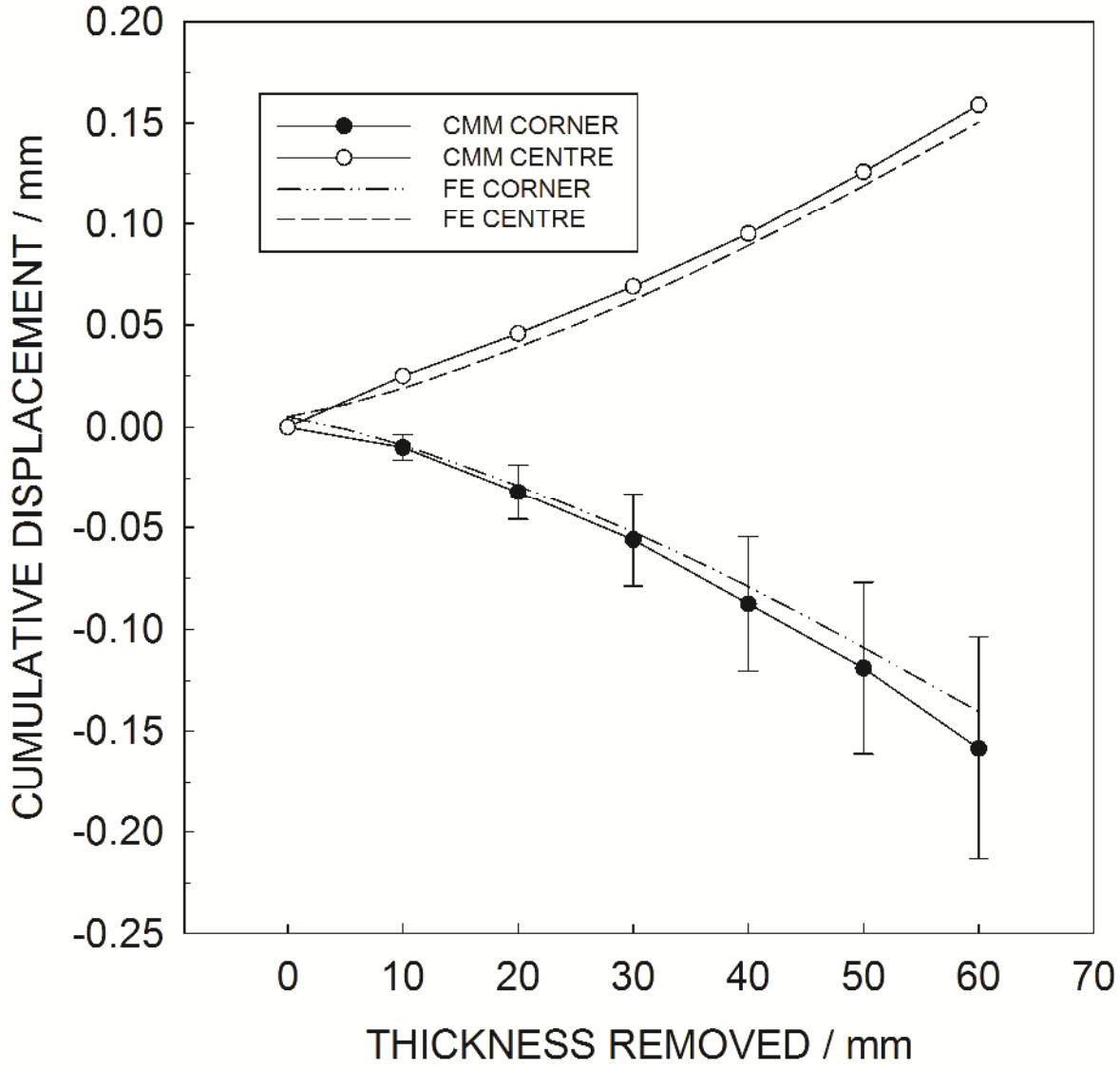

Figure 3 Cumulative displacement of two locations on the unmachined face of Block Z2RB as material is removed from the opposite face. CMM measurements compared to finite element prediction. Error bars for the CMM corner curve correspond to ±1 standard deviations for the mean of all four corner displacements.

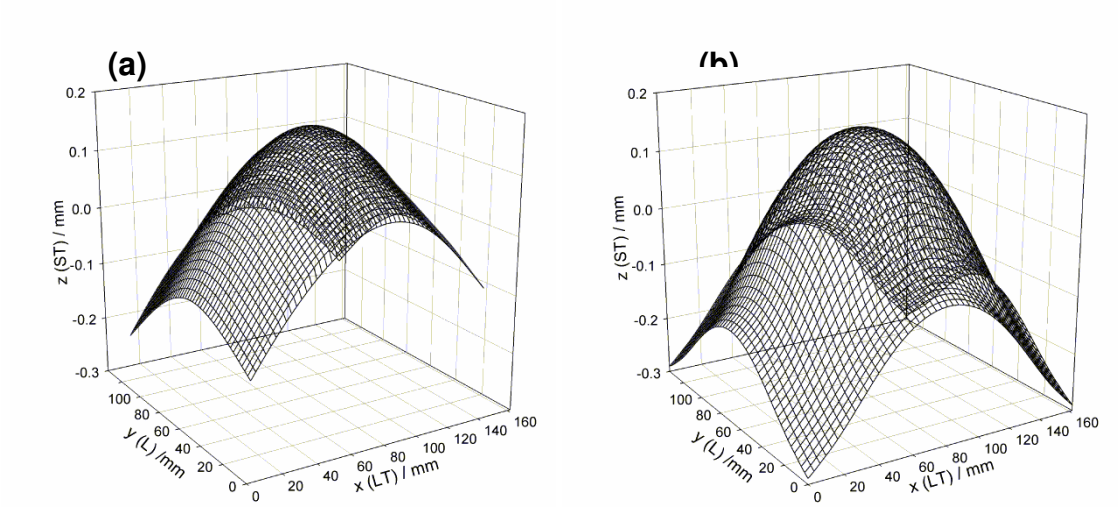

Figure 4 Distortion caused by removal of material to a depth of 60 mm (a) and corresponding FEA prediction (b)

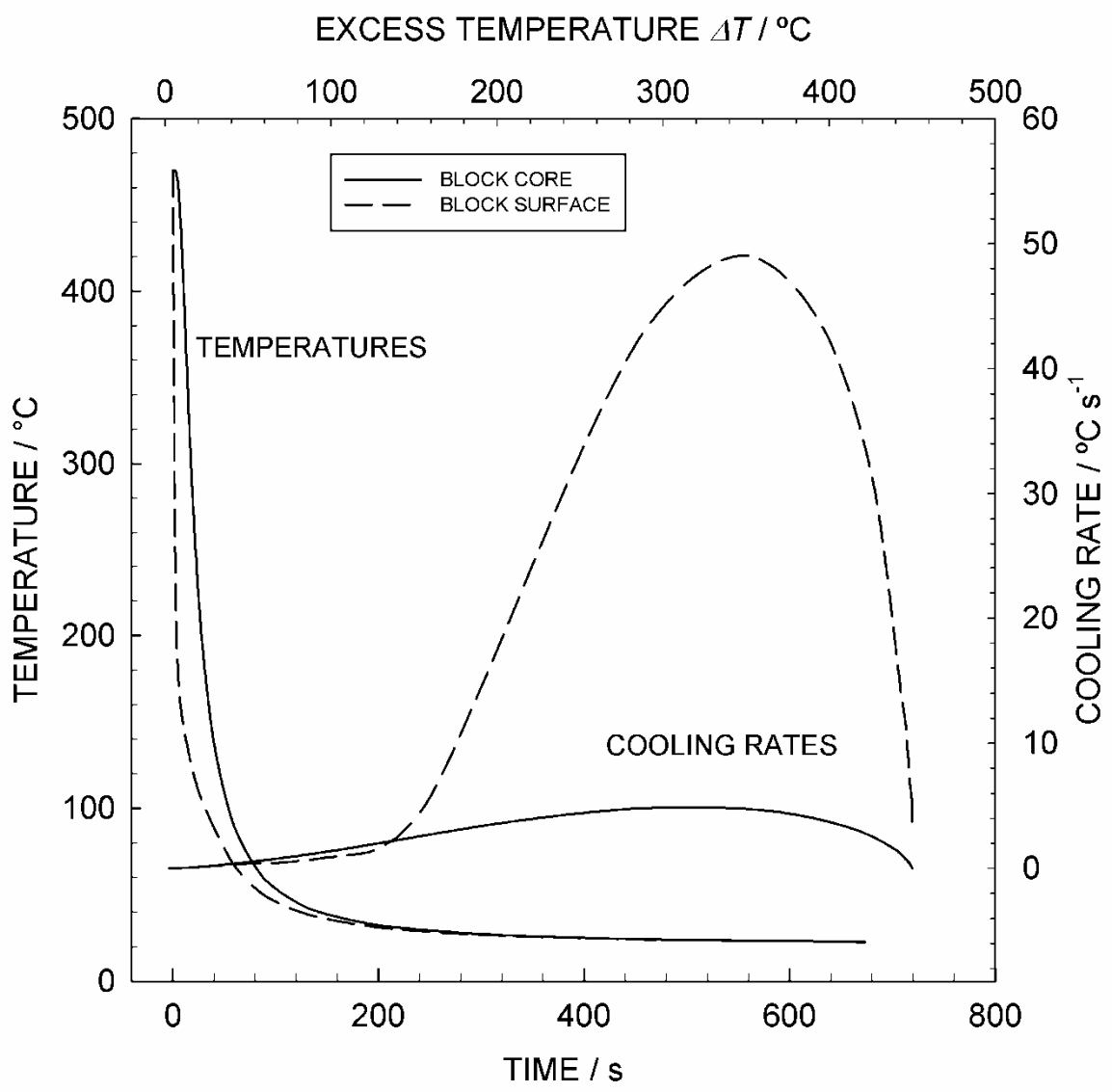

Figure 5 Predicted cooling curves and cooling rates during cold water quenching of one end of the strain free reference sample (surface) compared to the other (core).

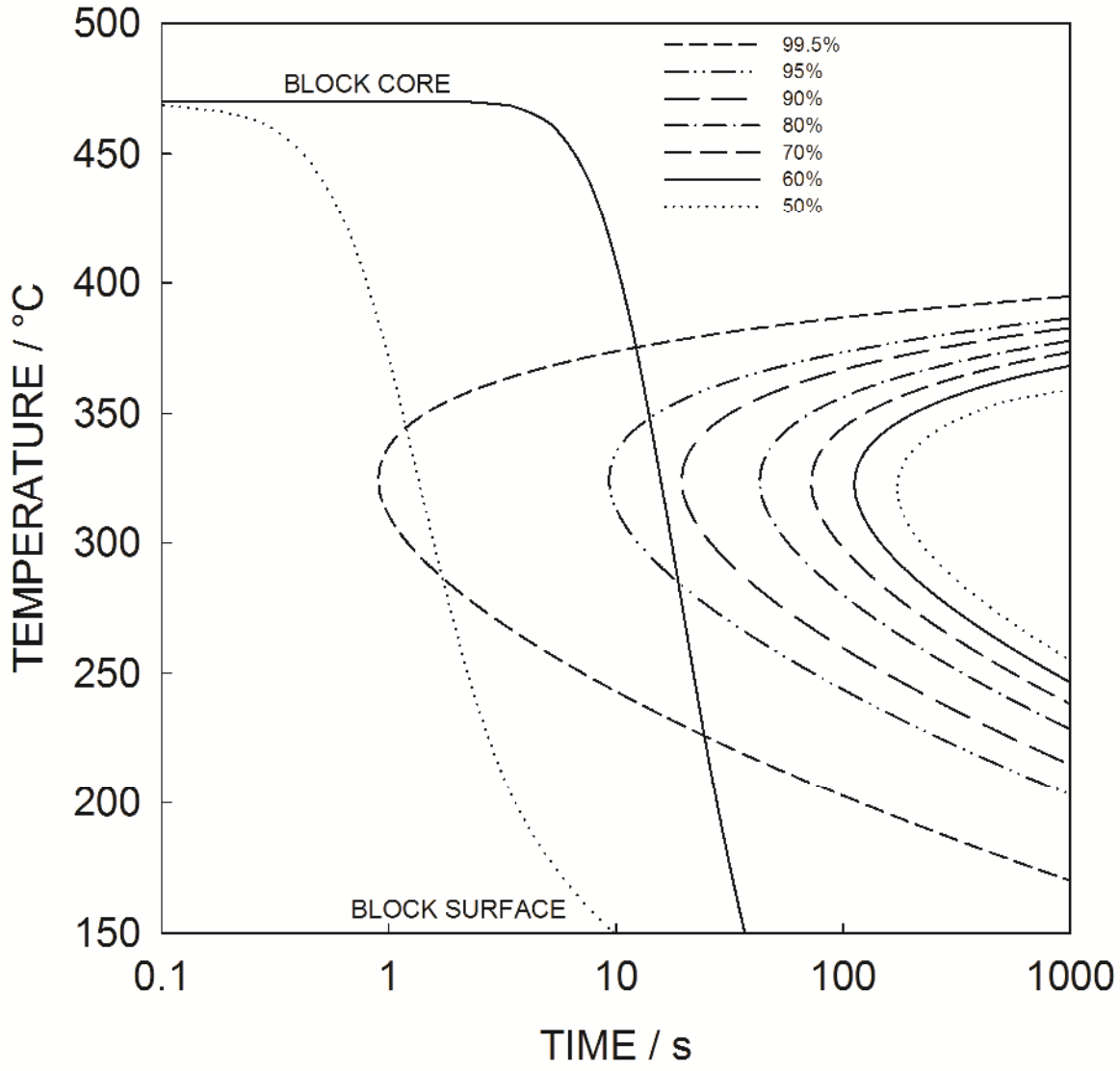

Figure 6 Time temperature transformation curves for the 7449 alloy. Each curve represents an iso-hardness curve for an over aged condition. Superimposed are the predicted cooling curves for the surface and core of the block during cold water quenching

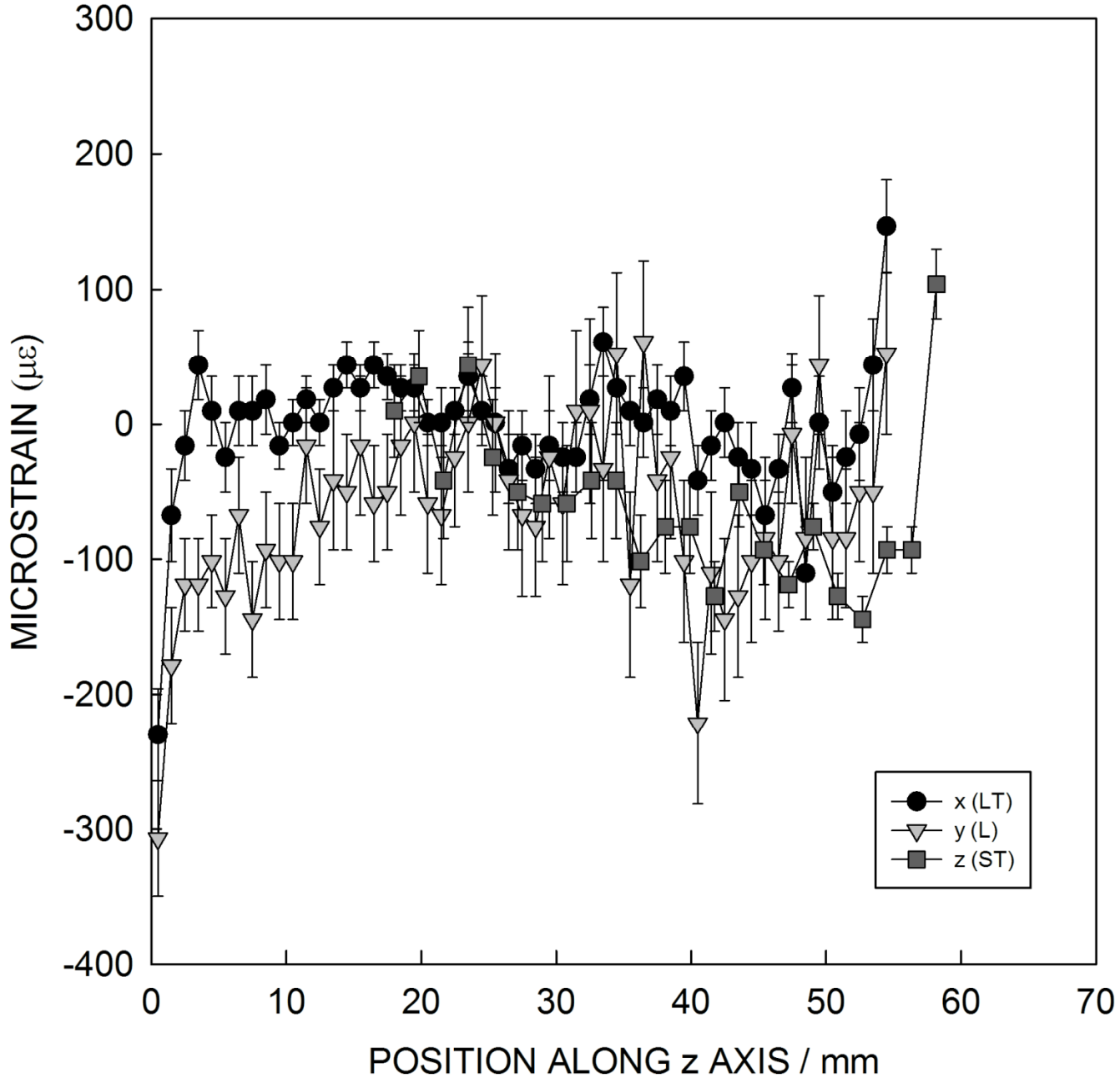

Figure 7 Strain free reference sample peak position displayed as variation of microstrain for the three orthogonal orientations

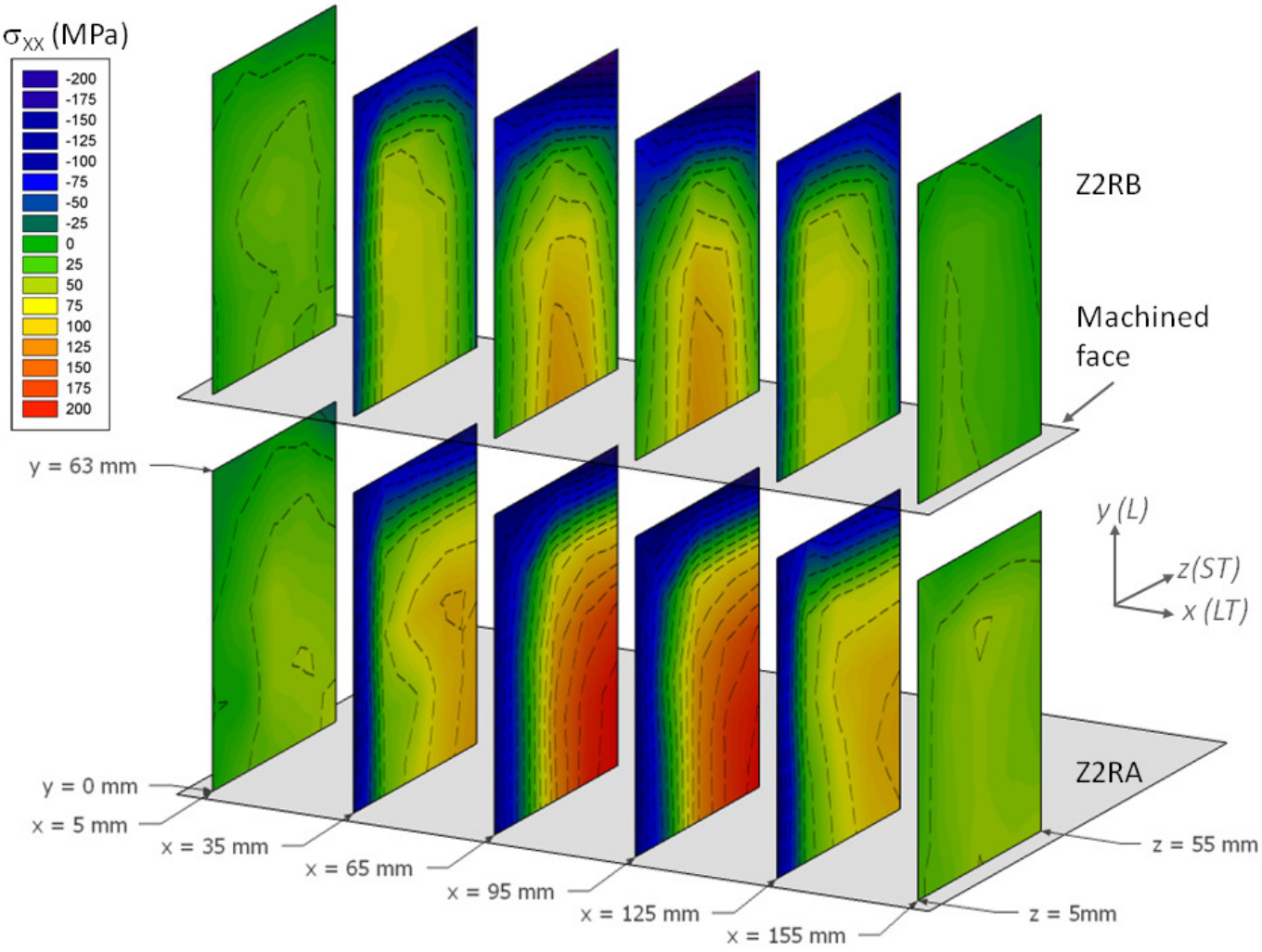

Figure 8 The σ_{XX} residual stresses in the unmachined block Z2RA (lower contour maps), and Z2RB (upper contour maps).

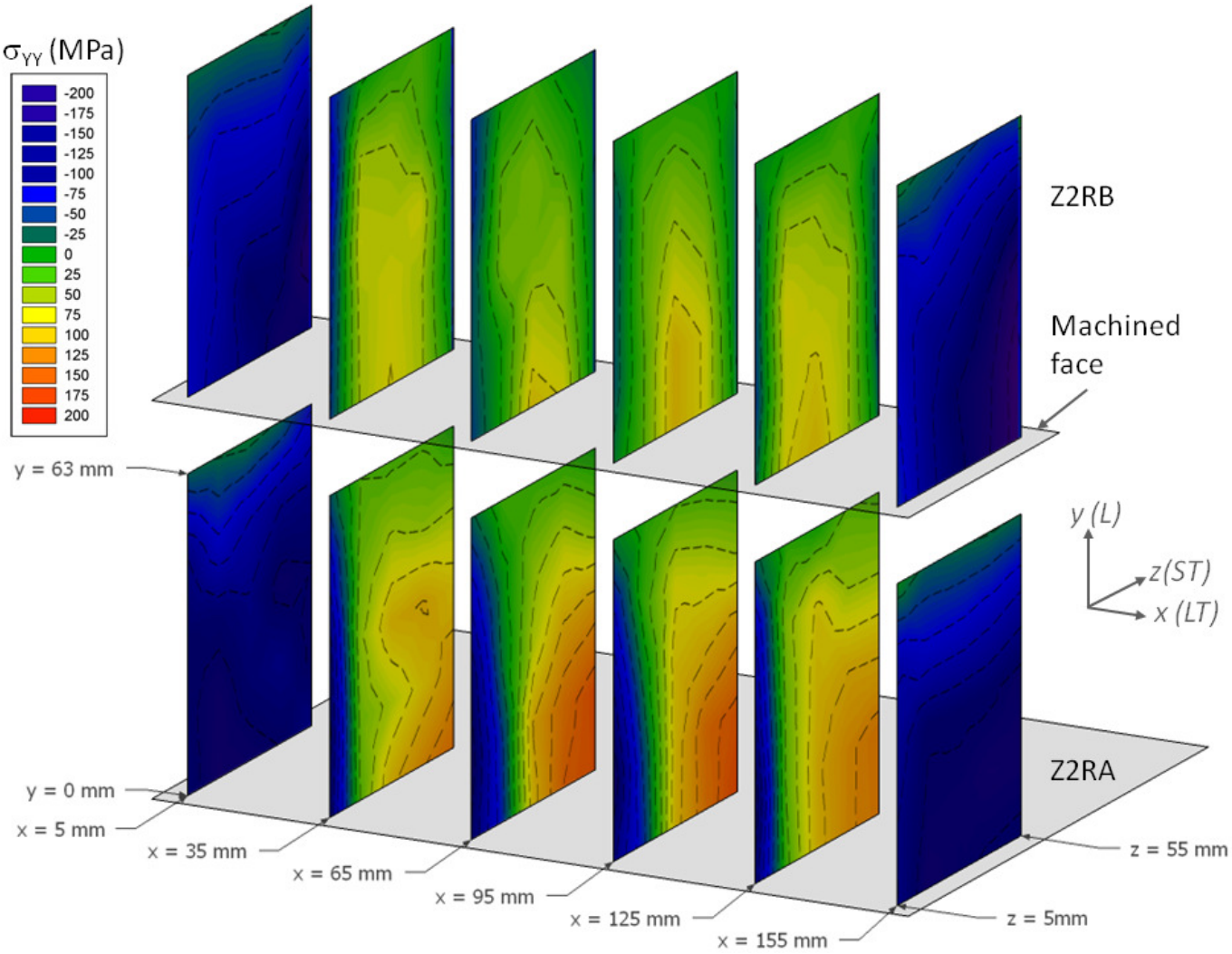

Figure 9 The σ_{YY} residual stresses in unmachined Z2RA (lower contour maps), and Z2RB (upper contour maps).

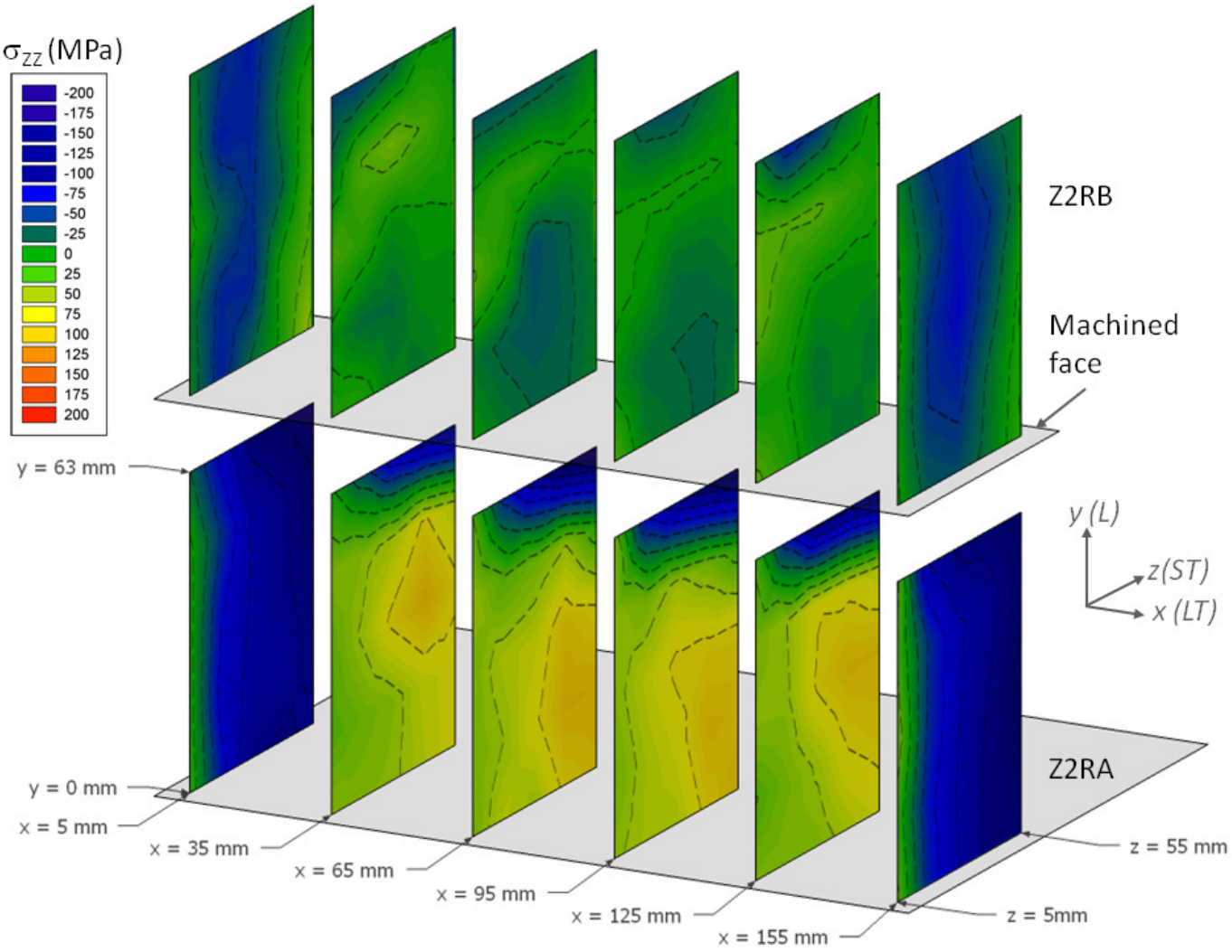

Figure 10 The σ_{zz} residual stresses in unmachined Z2RA (lower contour maps), and Z2RB (upper contour maps).

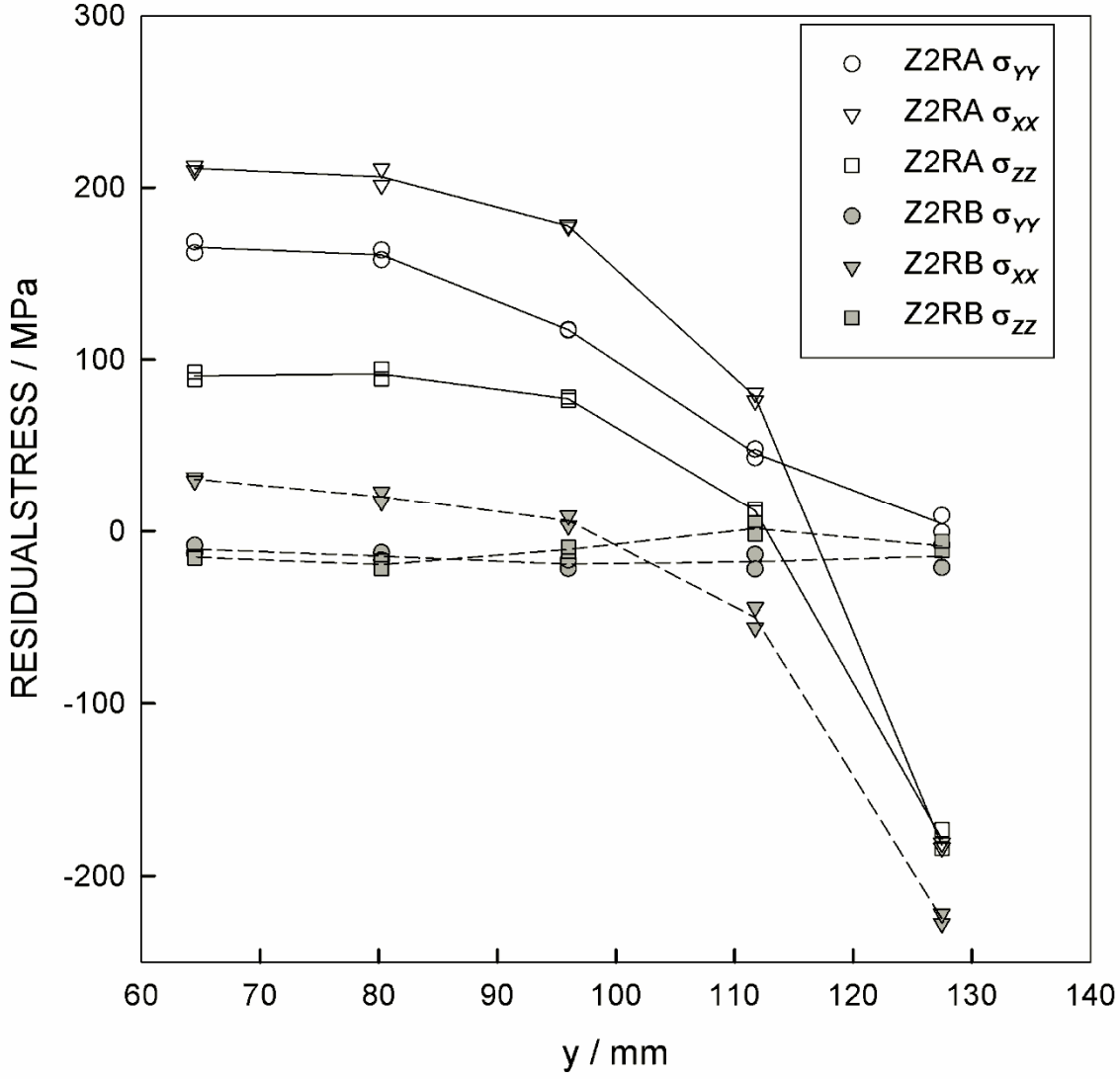

Figure 11 Variation of residual stress with position in the y (L) direction of block Z2RA and block Z2RB

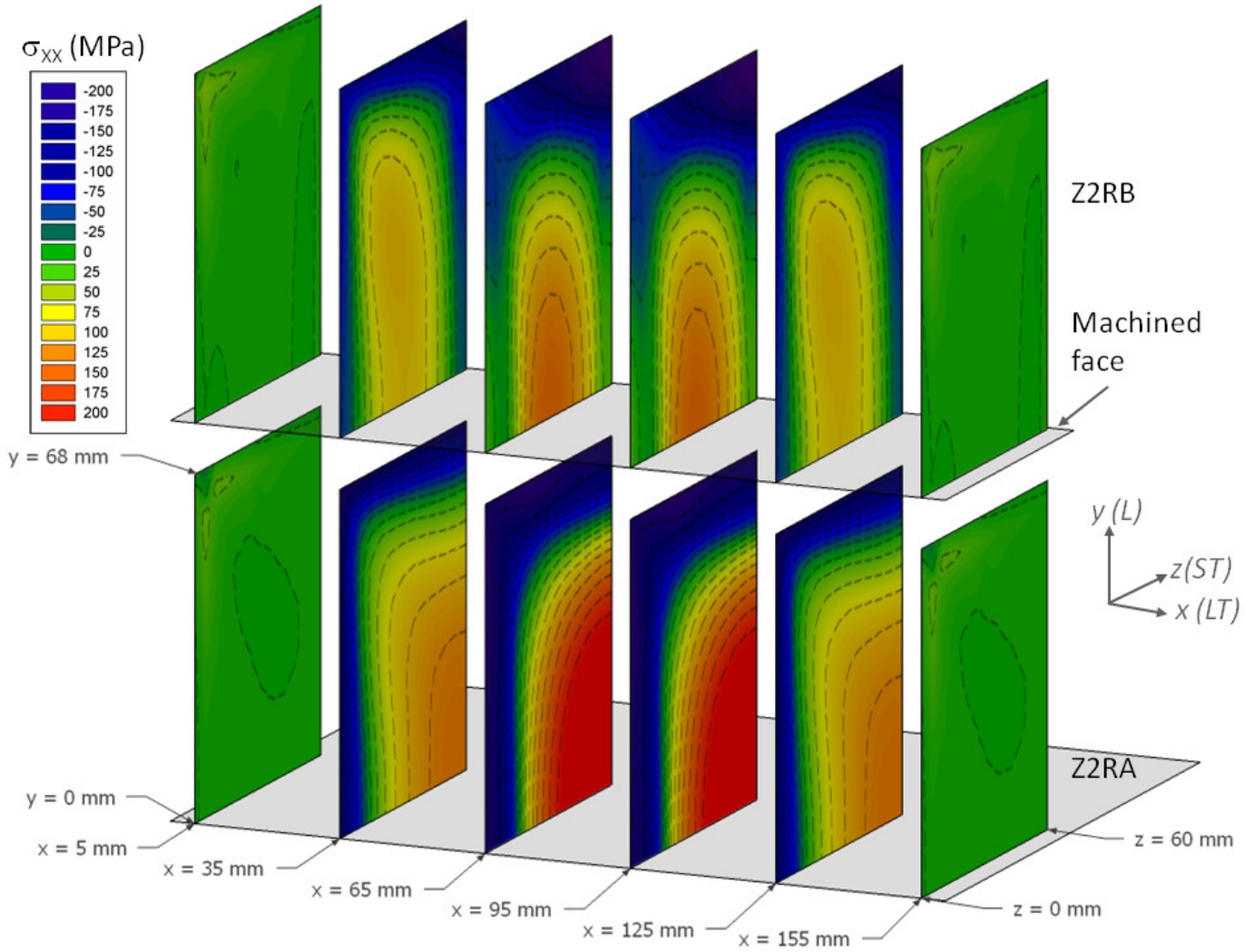

Figure 12 The FEA predicted σ_{xx} residual stresses in the unmachined block Z2RA (lower contour maps), and Z2RB (upper contour maps).

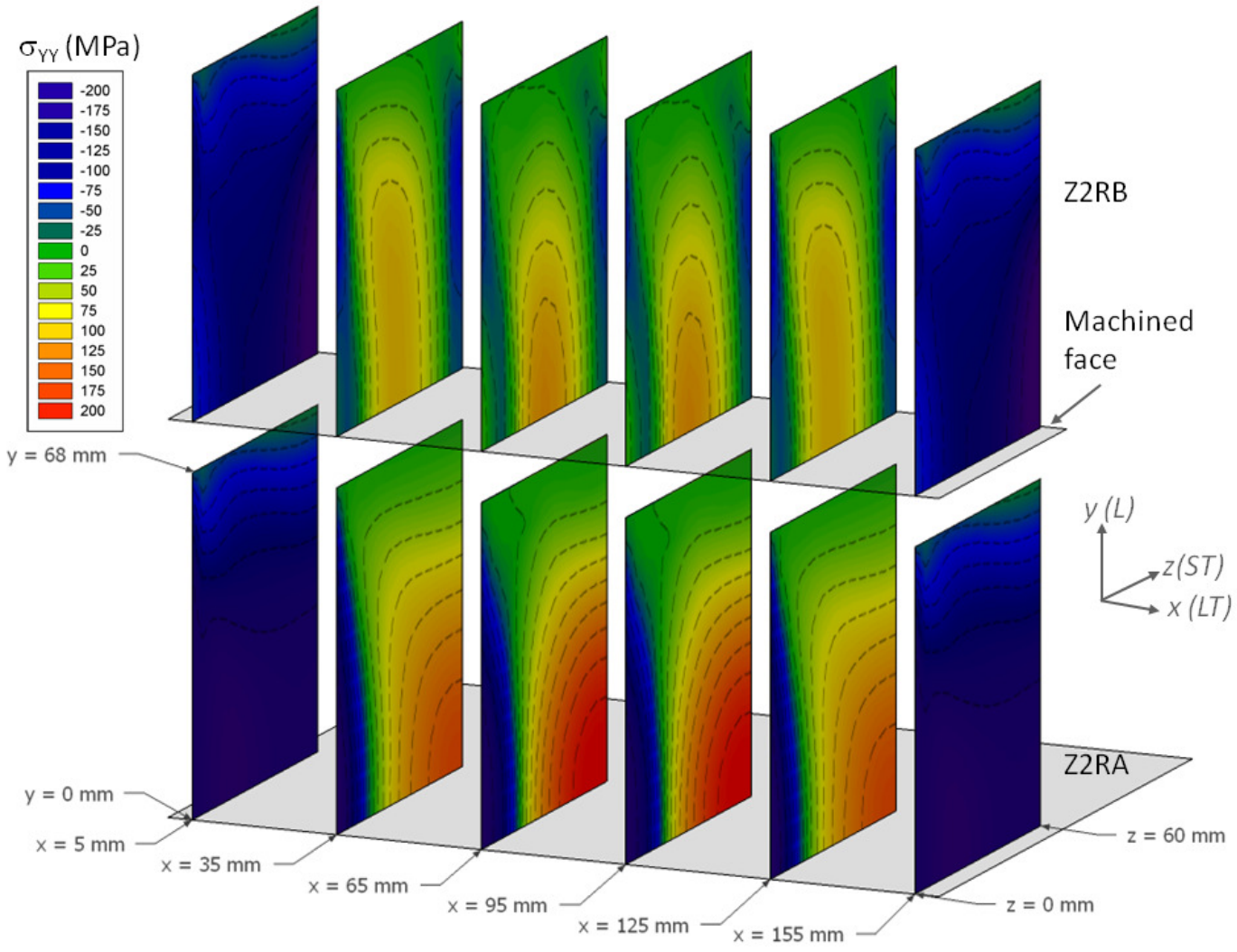

Figure 13 The FEA predicted σ_{YY} residual stresses in the unmachined block Z2RA (lower contour maps), and Z2RB (upper contour maps).

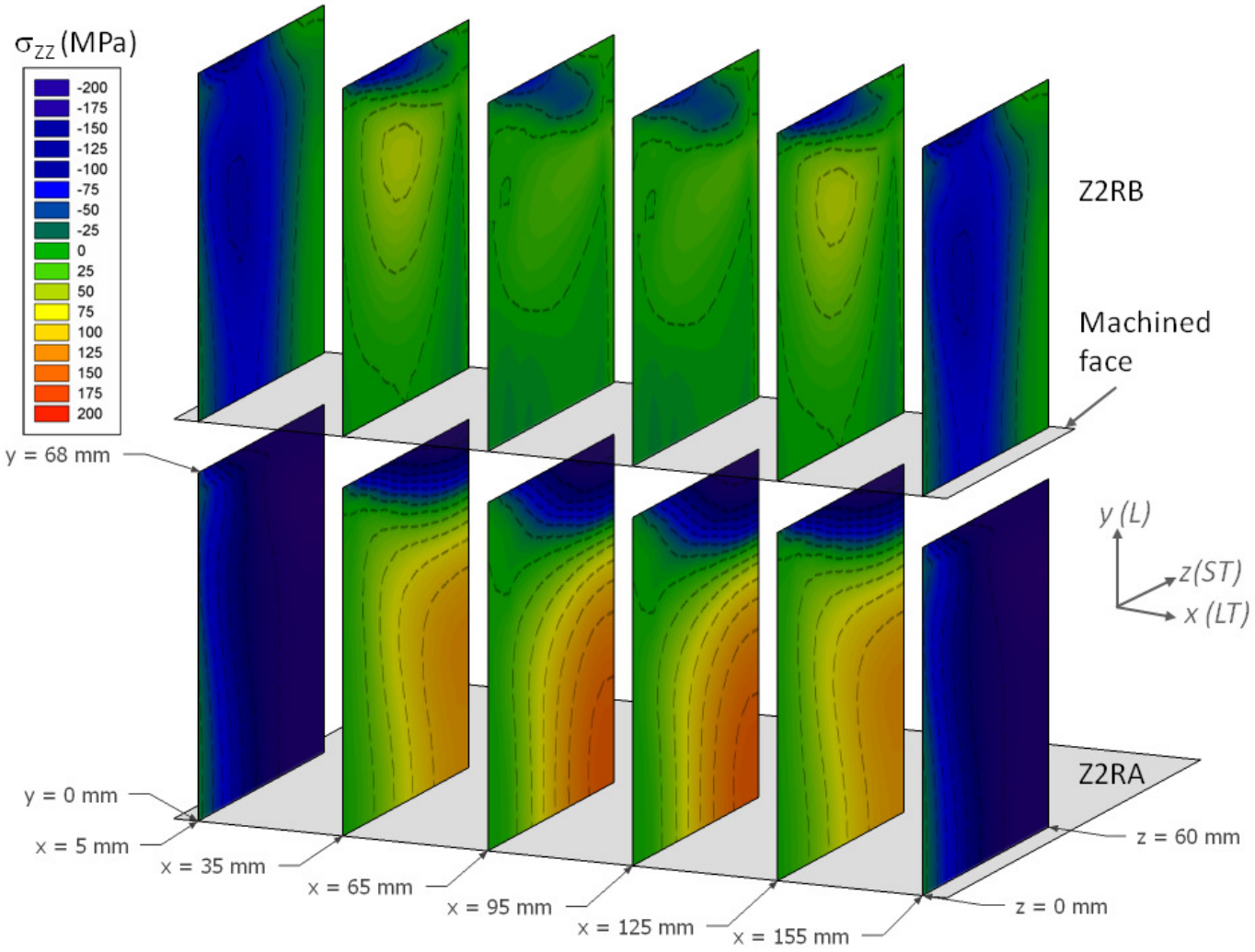

Figure 14 The FEA predicted σ_{zz} residual stresses in the unmachined block Z2RA (lower contour maps), and Z2RB (upper contour maps).